Unsteady hydrodynamics of tidal turbine blades

Citation for published version:
Thomas Scarlett, G & Viola, IM 2020, 'Unsteady hydrodynamics of tidal turbine blades', *Renewable Energy*, vol. 146, pp. 843-855. https://doi.org/10.1016/j.renene.2019.06.153

Digital Object Identifier (DOI):
10.1016/j.renene.2019.06.153

Link:
Link to publication record in Edinburgh Research Explorer

Document Version:
Peer reviewed version

Published In:
Renewable Energy

Unsteady hydrodynamics of tidal turbine blades

Gabriel Thomas Scarlett[a], Ignazio Maria Viola[a,*]

[a]*School of Engineering, Institute for Energy Systems, The University of Edinburgh, Edinburgh, EH9 3DW*

Abstract

Tidal turbines encounter a range of unsteady flow conditions, some of which may induce severe load fluctuations. Rotor blades can experience stall delay, load hysteresis and dynamic stall. Yet, the range of flow conditions which cause these effects for a full-scale axial-flow turbine are unclear. In this work we carry out a parameter study across a range of flow conditions by modelling root bending moment responses. We show how unsteadiness manifests along the span of the blade, the unsteady phenomena occurring and the conditions which induce the most significant load fluctuations. We find that waves and turbulence are the main sources of unsteadiness, and that extreme waves dominate over extreme turbulence. A yaw misalignment increases the load fluctuations but reduces the maximum peak. Large yaw angles, low tip-speed ratios, and very large waves lead to dynamic stall increasing the mean loads. Conversely, added mass effects mostly attenuate the loadings.

Keywords: unsteady hydrodynamics, tidal energy, dynamic stall, wave-induced loading, turbulence-induced loading, fatigue loading

1. Introduction

The ocean is inherently unsteady. Currents, waves, turbulence and the channel boundary layer present a challenging environment in which to deploy a tidal energy harvester. Tidal power generation is approaching a state of commercial readiness [1] with significant projects now underway [2]. Yet, questions remain regarding survivability [3, 4]. To be commercially viable devices must endure up to 25 years in the water without requiring major overhaul or repair.

*Corresponding author
Email address: I.M.Viola@ed.ac.uk (Ignazio Maria Viola)

As a rotor blade rotates through unsteady flow, large differences in the loads can occur compared to those experienced under steady conditions. A better understanding of the conditions that induce the most significant load fluctuations will improve the design and longevity of the device, which in turn will reduce the levelised cost of tidal energy.

The unsteady hydrodynamics of a tidal turbine blade depends on whether the flow is attached to, or separated from its surface. The latter induces moderate load oscillations, whereas the former can elicit significant fluctuations. In attached flow there are two interconnected flow phenomena. The first, known as the circulatory effect, arises when vorticity is shed from the trailing edge. This causes a change in the bound circulation around the foil and a subsequent amplitude reduction and phase lag in the lift response with angle of attack, compared to the quasi-steady value. The second, non-circulatory effect, also referred to as the added mass effect, is due to the time change in the pressure gradient over the foil. Unsteady separated flow is analogous with dynamic stall. This non-linear flow phenomenon manifests when unsteady separation and stall occur resulting in a clockwise hysteresis loop of the lift response with the angle of attack. Lift increases above the static stall angle as stall is delayed to a greater angle, then at a sufficiently large angle of attack a leading edge vortex may form and convect over the surface producing a further increase in lift. Unlike attached unsteady flow, lift fluctuations twice the static value can occur [5]. For a rotor blade the combination of blade rotation, which induces a centrifugal and Coriolis force on the flow, with dynamic stall can produce very large lift amplitudes compared to the non-rotational case [6, 7].

To date, the quantification of the unsteady loads incident to a tidal turbine rotor have been confined to scaled geometries, operating in simplified flows. Whelan *et al*. [8] carried out experiments on a scaled turbine in a towing tank. The turbine was towed at a uniform speed whilst oscillating the external carriage on which it was mounted. This generates oscillations in the rotor plane which are uniform with depth. In an attempt to quantify the circulatory and added mass contributions to the forces, the authors compared measured thrust data with Morrison's equation, which conveniently separates the added mass and drag force. Their study concluded that, for the range of frequencies tested, the added mass contribution was small. Milne *et al*. [9, 10] also carried out towing tank experiments and compared root bending moment measurements with Theodorsen's theory [11] which separates the circulatory and non-circulatory lift response. These results revealed that circulatory effects dominate over added mass effects at low frequencies.

With regard to separated flow, Milne *et al*. [9] determined that, at low tip-speed ratios, the flow was separated over most of the blade span, which for high frequency forcing caused the root bending moment to exceed the quasi-steady value by up to 25%. In a later study, Milne *et al*. [12] identified the key stages of dynamic stall in the root bending moment hysteresis. Galloway *et al*. [13] investigated the effects of a yaw misalignment and waves using a wave tank to generate linear waves. Results were compared with an in house blade-element momentum code, which included a dynamic stall and dynamic inflow correction. The experimental results revealed that the median value of the root bending moment was exceeded by up to 175% during the presence of large waves. The authors concluded that the effect of dynamic stall is limited and, therefore, can be neglected in some cases, despite not making comparison with quasi-steady values. In our recent study we quantified the loads for a full-scale, 1 MW horizontal axes tidal turbine operating in large wave conditions [7]. The loads, moments and power were modelled using measured flow velocity data from the European Marine Energy Center. The study revealed that, when operating at the optimal tip-speed ratio, separation and dynamic stall is confined to the blade root, which is in agreement with Galloway *et al*. [13]. However, reducing the tip-speed ratio led to increased flow separation and dynamic stall, which caused overshoots in the mean root bending moment compare to simple quasi-steady approximation. These latter findings concurs with the experiments of Milne *et al*. [12].

Overall, these past results show that, in some realistic unsteady flow conditions, the flow around the blade is dominated by dynamic stall, and this results in large load peaks and lower energy efficiency. However, there has yet to be a comprehensive study of global and local blade loadings for a broad range of flow conditions. In this paper we explore the different unsteady phenomena occurring along the blade span due to the shear layer, turbulence, waves and a yaw misalignment. Using our recently developed unsteady load model for arbitrary forcing [7], we identify the conditions which elicit the most significant load fluctuations and, for these conditions, how unsteadiness manifests along the span of the blade. We determine which blade section incurs the largest load fluctuations and whether added mass effects are amplifying or attenuating them.

2. Turbine specification

The dimensions of a 3-bladed, 1 MW tidal turbine representative of the Tidal Generation Ltd. DEEPGEN IV device deployed at the European Marine Energy Center (EMEC) test site during the ReDAPT project are considered. Schematic views of the port and front sides of the turbine are shown in Figure 1. A Cartesian coordinate system is placed at the still water level (SWL). The freestream current velocity is in the x direction, y is the port side direction and z is the vertical coordinate positive above the SWL. A cylindrical coordinate system with origin at the hub describes the radial (r) position along the blade, which extends to the tip ($R = 9$ m), and the azimuthal angle of the blade (ψ), which tracks the position of the blade as it rotates counter-clockwise from the z axis where $\psi = 0$. Also shown are the radius of the hub ($R_h = 1.0$ m), the water depth ($d = 45$m) and the distance from the hub to the SWL ($z_0 = 27$m). The chord (c) and geometrical twist (β_g) distributions along the blade span, follow those from Gretton [14]. This blade profile transitions to a circle at $0.13R$. We model all sections from $0.15R$ to the tip (R) with the NREL S814 geometry, which has a uniform maximum thickness in relation to the chord of 24%.

In a previous study the turbine was found to yield a peak power coefficient $C_P = 0.47$ when operating at a tip-speed ratio ($\lambda = 4.5$). Full details of this study can be found in Scarlett *et al*. [7]

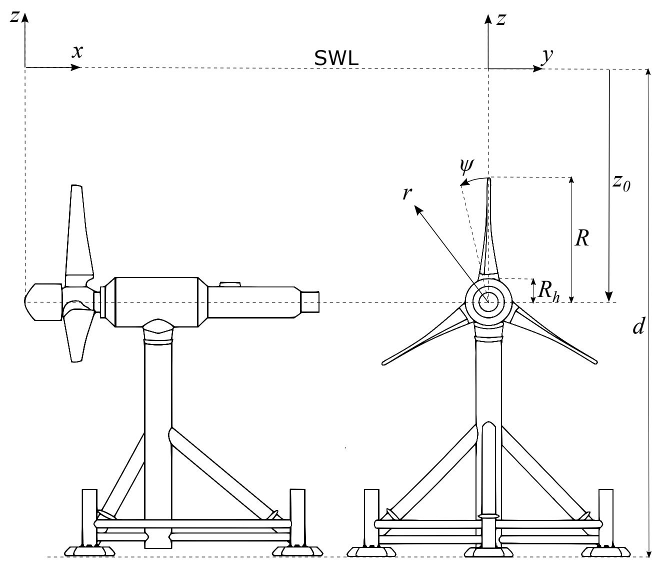

Figure 1: Schematic diagram of the tested tidal turbine.

3. Unsteady phenomena

The unsteady flow oscillations encountered by a tidal turbine blade vary in amplitude and frequency. As a blade rotates through the shear layer or during a yaw misalignment it will encounter a once (1P) or even twice (2P) per revolution load frequency response. Likewise, the rotor will sample waves and turbulence of varying amplitude and frequency. Long period waves of 10 s period, 5 m high waves addressed in our previous work can induce very large angles of attack [7]. The types of unsteady phenomena that materialise for a range of flow conditions are herein explained. These are split into attached and separated flow phenomena.

3.1. Attached flow

We investigate attached flow effects analytically for simple harmonic forcing using Theodorsen's theory [11] for a blade section and Loewy's theory [15] for a rotor blade.

Theodorsen provides the unsteady lift coefficient for a flat plate undergoing oscillations in angle of attack (α), pitch or plunge [11]. The solution is given explicitly, but restricted to pure harmonic forcing. Here we assume the forcing is pure α oscillations of the form $\alpha(t) = \bar{\alpha} + \alpha_0 e^{i2\pi f t}$, where $\bar{\alpha}$ is the mean value, α_0 the amplitude, f the forcing frequency and t is time. Theodorsen's solution is then

$$C_L = [i\pi k + 2\pi C(k)]\alpha(t). \tag{1}$$

The first term in Equation 1 is the non-circulatory, added mass effect, and the second term, is the circulatory effect. $C(k)$, which multiplies the circulatory term is Theodorsen's complex transfer function, defined as

$$C(k) = \frac{H_1^{(2)}(k)}{H_1^{(2)}(k) + iH_0^{(2)}(k)}, \tag{2}$$

where $H_v^{(2)} = J_v - iY_v$ is a Hankel function of the second kind; J_v and Y_v are Bessel functions of the first and second kind respectively; v refers to the order, which in this model takes either the value 0 or 1. The argument k is the reduced frequency, a non-dimensional parameter that is a measure of the unsteadiness. In general, the flow is said to be unsteady if $k > 0.05$, and highly unsteady for $k > 0.2$ [16]. The reduced frequency is defined as

$$k = \frac{\pi f c}{U_r}, \tag{3}$$

where U_r is the relative velocity.

Using Theodorsen's theory we investigate how the lift response varies at a blade section near the tip ($r \approx 0.98R$ and $c \approx 0.8$ m), where the flow is attached. Three values of k are simulated: $k = 0.07$, $k = 0.16$ and $k = 0.31$. Representing a 10 s period wave, a 1P and a 2P forcing, respectively. The turbine is operating at the optimum $\lambda = 4.5$. For each case we assume a moderate forcing $U_r = 7.0$ ms^{-1}, $\alpha_0 = 4°$, and $\bar{\alpha} = 5°$. The results are shown in Figure 2, alongside the quasi-steady value ($2\pi\alpha$) corresponding to $k = 0$, for comparison. We observe that the unsteady responses are counter-clockwise hysteresis in C_L with α, and that there is an amplitude reduction and phase lag compared to the quasi-steady value, which for this k range decreases inversely with k.

Theodorsen's model conveniently separates the circulatory and non-circulatory components, enabling the contribution of each to the total C_L response to be

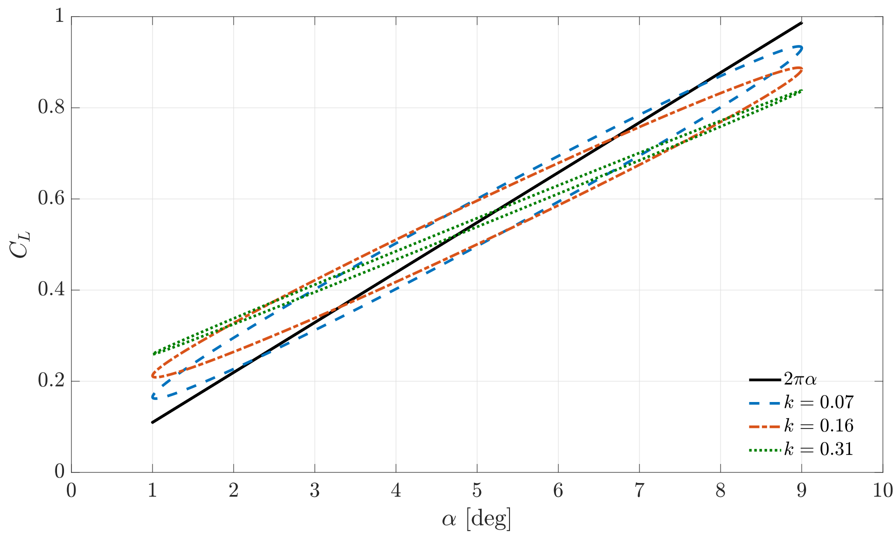

Figure 2: Unsteady lift coefficient given by Theodorsen for a section near the tip of the blade. The static linear value ($2\pi\alpha$) is shown for comparison.

quantified. Defining the normalised lift coefficient amplitude (ζ) as

$$\zeta = \frac{|C_L|}{2\pi|\alpha_0|} = |(F + iG) + i\frac{k}{2}|, \tag{4}$$

where the first and second terms are the circulatory and added mass components respectively, $F = \mathrm{Re}(C(k))$ and $G = \mathrm{Im}(C(k))$. In Figure 3(a) the contribution to ζ is shown for $k \in \{0, ..., 4\}$. We find that if $k \leq 1.8$ then $\zeta < 1$, however, when $k > 1.8$, the amplitude exceeds the steady value ($\zeta > 1$) and then increases with k, approaching the added mass linear response in the limit. Figure 3(b) shows a magnification of the region $k \in \{0, 1\}$, which is the range in which a a tidal turbine operates. Interestingly in the interval $[0 < k < 0.56]$, added mass dampens the total response. This is because the circulatory and added mass components are combined vectorially. Since tidal turbines mostly operate within this interval, added mass effects are unlikely to become a problem. This is important since it has been suggested [8, 17] that the high density of water might lead to significant added mass effects for tidal turbines. However, this is not the case as long as $k < 0.56$. Conversely, the circulatory response, associated with dynamic inflow, is the significant effect, which concurs with the scale model

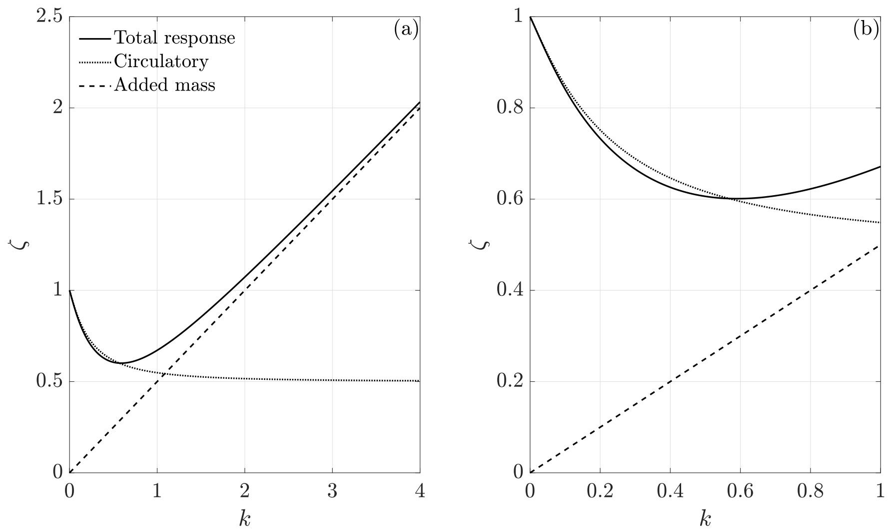

Figure 3: Normalised amplitude of the total, circulatory and non-circulatory coefficients with reduced frequency for pure angle of attack oscillations.a, full range, b, tidal turbine range.

results of Milne *et al*. [9]. Clearly the observation from Figure 2, that the amplitude reduces inversely with k, are only true inside the interval $[0 < k < 0.56]$. For $k > 0.56$ the relationship inverts.

Loewy [15] addressed the problem of a helicopter rotor in hover, where a blade section may encounter its own returning vorticity and that of neighbouring blades. The solution was to modify Theodorsen's function with a new term. This term modifies C_L depending on k, the wake spacing (h_w) and the frequency ratio ($m = f/f_r$), where f_r is the rotational frequency of the rotor. A tidal turbine is analogous to a helicopter rotor in hover, however, the wake convects with the mean velocity rather than the induced downwash.

In Loewy's model C' is used in place of C in Equation 1, where

$$C'(k, W) = \frac{H_1^{(2)}(k) + 2J_1(k)W}{H_1^{(2)}(k) + iH_0^{(2)}(k) + J_1(k) + iJ_0(k)W}, \tag{5}$$

and Loewy's function (W) is defined

$$W(k, h_w, m) = (e^{kh_w} e^{i2\pi m/N_b} - 1)^{-1}, \tag{6}$$

where N_b is the number of blades. The wake spacing parameter is

$$h_w = \frac{2v_i}{f_r N_b c}, \tag{7}$$

where v_i is the averaged wake convection velocity. For a helicopter rotor, v_i is the average induced downwash, whereas for a tidal turbine it is the streamwise velocity. From actuator disc theory, the convective velocity at the blade is $U_0(1-\bar{a})$, where U_0 is the mean current velocity and $\bar{a}$ is the mean axial induction factor. In the far wake, the convective velocity is $U_0(1-2\bar{a})$. A simple linear average between the two velocities gives

$$v_i = U_0\Big(1 - \frac{3}{2}\bar{a}\Big). \tag{8}$$

In Figure 4, hysteresis loops of C_L are precicted for a section near the tip using both Loewy and Theodorsen' models. The predictions are compared for $k \in \{0.07, 0.16, 0.24, 0.31, 0.47, 0.72\}$. For each case we assume $\alpha_0 = 4°$, $\bar{\alpha} = 5°$, $\lambda = 4.5$, $U_0 = 2.7$ ms^{-1}, $\bar{a} = 0.3$ and $U_r = 7.0$ ms^{-1}. We observe that as k increases, the phase lag and amplitude reduction from $2\pi\alpha$ also increases. For the lowest k, corresponding to a large 10 s wave, we observe that the width of the hysteresis ellipse predicted by Loewy is reduced compared to Theodorsen's prediction. However, the amplitude is slightly increased. The amplitude predicted by Loewy continues this trend until $k = 0.31$, which corresponds to a 3P forcing. For larger k there is a greater added mass contribution and the difference between the two theories becomes negligible. Thus, for this turbine and operating conditions, a slight increase in the amplitude of C_L is expected for $k < 0.3$ due to returning and neighboring wakes.

3.2. Separated flow

Dynamic stall is when unsteady separation and stall occurs, resulting in a clockwise hysteresis loop of C_L with α. Unlike attached unsteady flow, large fluctuations above static C_L can occur. There are two dynamic stall regimes: light stall and deep stall. Under light dynamic stall, moderate oscillations around the static stall angle (α_{ss}) occur. The unsteady motion causes stall delay, a process

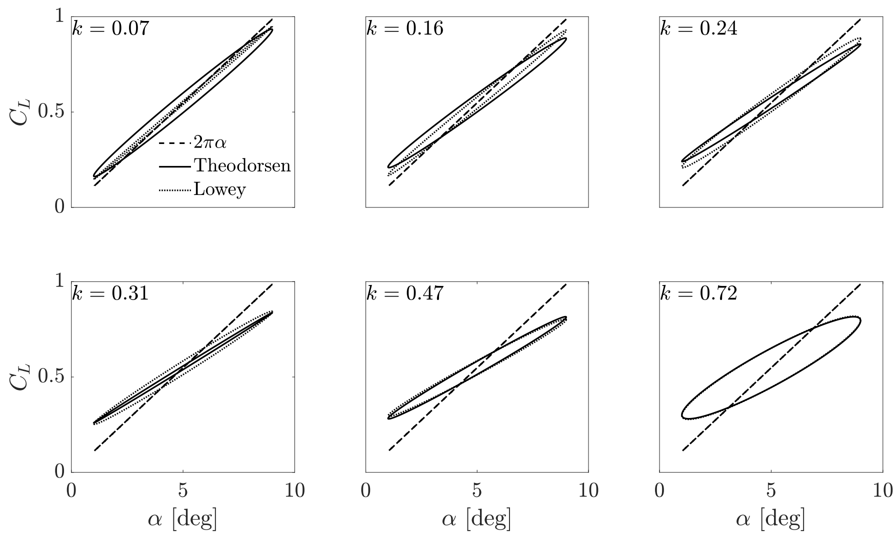

Figure 4: Unsteady lift coefficient given by Theodorsen and Loewy for a section near the blade tip for a range of oscillation frequencies.

whereby the angle of attack increases sufficiently rapidly such that separation is prevented beyond α_{ss}, and C_L increases beyond the maximum static value. In deep dynamic stall the oscillations far exceed α_{ss} and the critical α for dynamic stall is attained, at which point a leading edge vortex (LEV) forms, detaches and convects downstream. The convection of the LEV over the surface can produce load overshoots of 100% or more above the quasi-steady value [18].

Dynamic stall load hysteresis loops are predicted using the model of Sheng *et al.* [19], with a modification to account for rotational augmentation using the model of Lindenburg [20]. Full details of the model, including a validation case are described in Scarlett *et al.* [7]. Figure 5(a) shows representative load hysteresis at a mid-blade section where $r \approx 0.56R$ and $c \approx 1.26$ m, for a harmonic forcing, $f = 0.1$ Hz, $\alpha_0 = 5°$ and $\bar{\alpha} = 10°$. We observe that C_L increases linearly past $\alpha_{ss} \approx 12°$, until the end of the cycle, then C_L lightly stalls and returns to the static value. In Figure 5(b) the load hysteresis loop is shown for a blade section near the root where $r \approx 0.15R$ and $c \approx 1.6$ m. A larger $\alpha_0 = 10°$ and $\bar{\alpha} = 14°$ occur due to the reduced tangential velocity here which

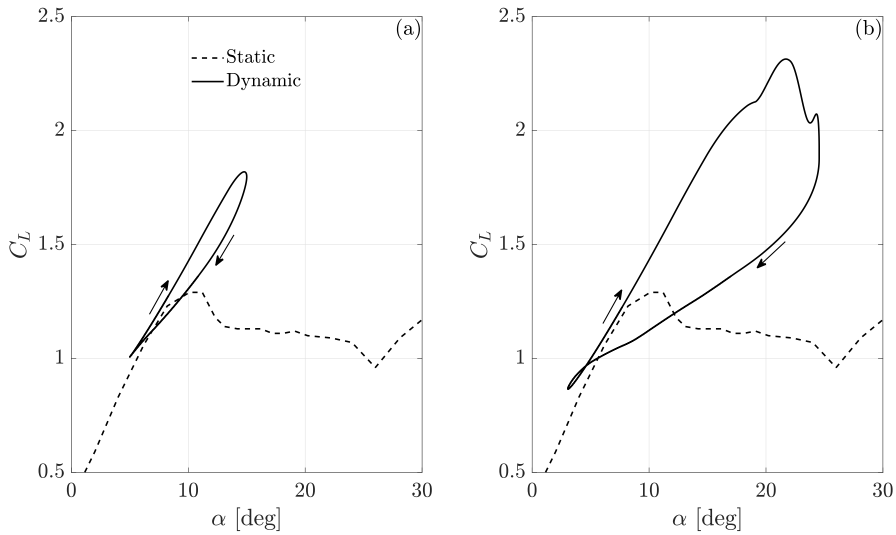

Figure 5: Unsteady lift coefficient with angle of attack for (a) light dynamic stall and (b) deep dynamic stall.

increases the flow angle. C_L increases linearly above α_{ss} until $\alpha \approx 19°$, which is the critical angle for dynamic stall. The flow then separates at the leading edge, and there is a build up of circulation into a concentrated vortex. A LEV then detaches and convects over the chord, producing a load overshoot more than twice the quasi-steady value. The vortex sheds near the trailing edge and stall occurs. However, as α continues to increase, a secondary vortex forms, producing a slight C_L recovery at $\alpha \approx 23°$. Deep stall then occurs and C_L rapidly decreases. Once α becomes sufficiently small, the flow reattaches.

4. Global blade response to unsteady flow conditions

In this section we investigate the wide range of unsteady flow conditions which a tidal turbine blade may encounter. Firstly, individual 1P, turbulence and wave forcings are considered. These results are used to select combined realistic flows which are further examined. The responses are categorised by the standard deviation of the root bending moment coefficient (C_{M_y}), defined as

$$C_{M_y} = \frac{2M_y}{\pi R^3 \rho U_0^2}, \tag{9}$$

where ρ is the fluid density. Events where the mean root bending moment coefficient exceeds the quasi-steady counterpart ($C_{M_y q.s}$) are identified by isolines of the ratio ($\bar{C}_{M_y}/\bar{C}_{M_y q.s}$). This will indicate the extent to which dynamic stall is having a global effect.

Simulations are carried out using our unsteady tidal turbine model which is described in detail in Scarlett *et al*. [7], and freely available to download from our GitHub repository [21]. There is a blade-element momentum implementation using the solution method of Ning [22]. The unsteady loads are determined in the time domain for any arbitrary forcing. The model comprises of an attached load model using the time-domain solution of Wagner [23], which is synonymous with Theodorsen's frequency-domain solution, and a dynamic stall implementation which is based on the model of Sheng *et al*. [19]. A modification is made to account for rotational augmentation using the model of Lindenburg [20]. It is important to note that the attached flow solution is part of the nonlinear dynamic stall solution. When the flow remains attached, the solution tends to Theodorsen's solution. However, any arbitrary forcing can be considered. Unfortunately, there is no time domain equivalent of Loewy's solution, thus returning wakes are not taken into account. However, we have seen in section 3 that they are a minor concern compared to separated flow phenomena. The quasi-steady value is predicted using static wind tunnel measurements of the force coefficients [24].

4.1. Once per revolution forcing

A once per revolution forcing due to the rotation of the blade through the shear flow and a yaw misalignment is considered. The shear flow is associated with the tidal channel boundary layer. The horizontal current velocity u_x is non-uniform with depth due to the presence of the bed, which causes a reduction in the velocity profile with depth. At the bed there is no slip ($u_x(-d) = 0$). At the still water level we set $u_x(0)= U_\infty$. The u_x profile is then defined using a power law approximation:

$$u_x = U_\infty \left(\frac{z+d}{d}\right)^\nu, \tag{10}$$

for $-d \le z \le 0$. In this study $\nu = 1/7$, which was found to be a reasonable estimate of the time-averaged velocity profile within the depth range of a turbine operating at EMEC [7]. If the turbine is yawed relative to the freestream at a yaw angle (γ) the streamwise velocity is reduced by $\cos(\gamma)$ and a tangential, azimuthally varying component; $u_x \sin(\gamma)\cos(\psi)$ appears. In addition, blade sections downstream relative to the center of the hub, encounter more of the wake, therefore, a greater induced velocity. Conversely, blade sections upstream of the hub, outside of the wake encounter a lower induced velocity. We incorporate this effect into the axial induction factor using the uncoupled approach given by Ning *et al*. [25], which post corrects a after the blade-element momentum algorithm converges for zero yaw. The tangential induction factor remains unchanged. The corrected induction factor is

$$a_\gamma = a\left(1 + \frac{15\pi}{32}\mu \tan\chi \cos\psi\right), \tag{11}$$

where χ is the wake skew angle which is approximated as $\chi \approx (0.6a + 1)\gamma$ [26].

A range of 1P inflow conditions, $U_0 \in \{1.2, 3.5\}$ ms^{-1}, $\lambda \in \{3, 7\}$ and $\gamma \in \{0, 180°\}$ are simulated over 50 rotations. For each flow condition the standard deviation of the root bending moment ($\sigma_{C_{M_y}}$) is predicted. The results displayed in Figure 6 show that, $\sigma_{C_{M_y}}$ increases with γ and the inverse of λ. At low λ, dynamic stall effects the mean loads, even when the only source of unsteadiness is the rotation through the shear layer. This is evident by the 1.00 isoline indicating the boundary where $\bar{C}_{M_y}/\bar{C}_{M_y(q.s)}$ becomes positive for the $\gamma = 0$ case. The range increases to $\lambda \approx 4$ for $\gamma = 40°$, and $\lambda \approx 4.5$ for the largest $\gamma = 50°$ case. However, as γ increases the ratio decreases, with no values above 1.10 occurring for $\gamma > 20°$. At high λ, added mass effects result in lower C_{M_y} compared to the quasi-steady counterpart. However, we found that the ratio is never below 0.95, and hence no isolines of values below unity are displayed.

Thus, at low λ, unsteady conditions will always increase the mean loads compared to a quasi-steady prediction. This is due to the slower rotational speed, which reduces the tangential velocity, which increases α. As α increases along the blade, dynamic stall becomes the dominant loading regime. This has previously been reported for large wave induced loads when operating at lower, sub-optimal values of λ [7]. These results show that the yaw misalignment must be extremely significant to affect the mean loads at the optimal λ.

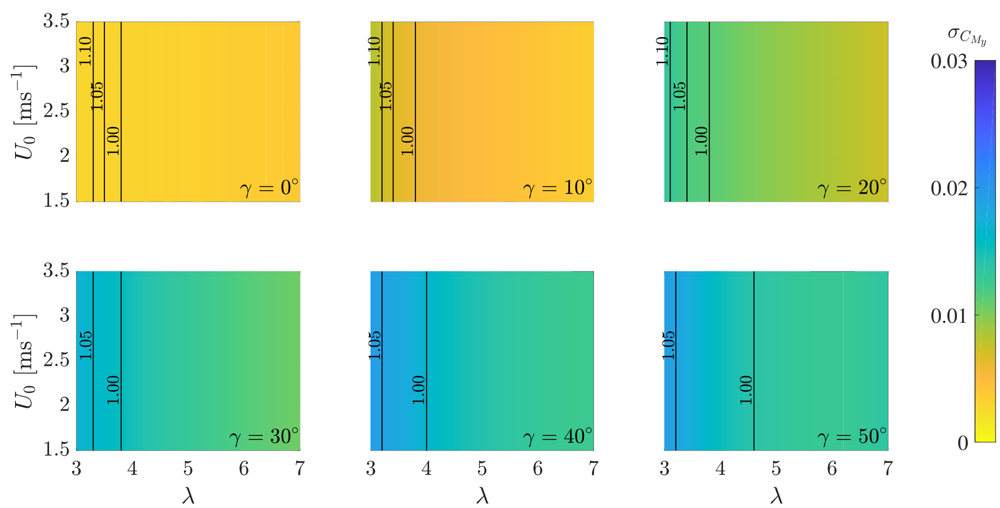

Figure 6: Filled contour map showing the standard deviation of the root bending moment due to varying current velocity, tip-speed ratio and yaw angle. Solid contour lines show the ratio between the mean root bending moment and the quasi-steady counterpart.

4.2. *Turbulence forcing*

Turbulent velocity fluctuations are synthesised using the von Kármán atmospheric turbulence spectrum [27], which has widely been used in wind engineering and wind energy research [26]. State of the art spectral methods simulate spatially coherent, three-dimensional turbulence. However, this requires spatial correlations of the flow, which, to date have not been recorded for tidal channel turbulence. Therefore, in this study we assume that turbulence is spatially uniform.

The streamwise synthetic velocity spectra S_x is defined as

$$S_x = \frac{4L_x\sigma_x}{U_0}\frac{1}{(1+70.7n^2)^{\frac{5}{6}}}, \tag{12}$$

where L_x is the length scale in meters; σ_x is the standard deviation defined as $\sigma_x = I_x U_0$, where I_x is the streamwise turbulent intensity; $n = L_x f_t/U_0$ and f_t is the turbulent frequency component. The velocity spectra in the y-direction is

$$S_y = \frac{4L_y\sigma_y}{U_0}\frac{1+753.6n^2}{(1+282.8n^2)^{\frac{11}{6}}}, \tag{13}$$

where $\sigma_y = R_t\sigma_x$, $L_y = R_t L_x$ and R_t is the anisotropy ratio. For $R_t = 1$, turbulence is isotropic and anisotropic if $R_t < 1$. Here we assume $S_z = S_y$. Velocity time series are simulated using the method of Shinozuka [28]:

$$u_i = \sqrt{2\Delta f_t}\sum_{j=1}^{N}\sqrt{S_{ij}}\cos\bigl(2\pi f_{t_j}t + \Phi_j\bigr), \tag{14}$$

where i denotes x, y or z; Δf_t is the frequency spacing, N the number of f_t components and Φ is the phase angle, which is a uniformly distributed random variable between 0 and 2π. The velocity time series generated using the Shinozuka method was found to conserve the input standard deviation to the von Kármán spectrum and to be approximately normally distributed.

Recent characterisation studies of the turbulent flow structure at the Sound of Islay ascertained that the von Kármán spectra predicted well the measured velocity spectra [29, 30]. Here we compare the streamwise velocity spectra measured at EMEC with that predicted using the von Kármán spectra. Measurements were recorded using a Single-Beam Acoustic Doppler Profiler at a sample rate of 4 Hz, full details of the data acquisition method can be found in Sellar *et al*. [31]. The flow sample was measured during flood tide with no waves present. The location $x = -20$ m, $y = 0$ m and $z = -27$ m, corresponds to hub height. The measured flow statistics are: $U_0 = 2.74$ ms^{-1}, $I_x = 9\%$ and $L_x = 26.5$ m. In Figure 7, the modelled spectra fits the measured data well. Doppler noise from the instrument distorts the measurements from about 0.5 Hz, without this the profile would continue along the 5/3 slope or decrease.

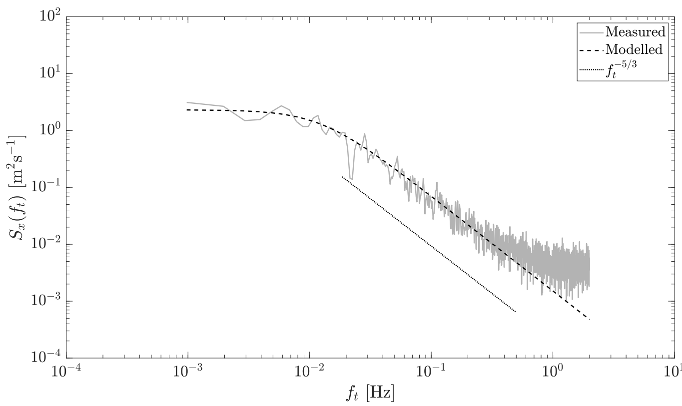

Figure 7: Comparison of the measured and modelled streamwise velocity spectra from the European Marine Energy Center in Orkney.

A range of turbulent parameters, $I_x \in \{5, 20\}$%, and $R_t \in \{0.5, 1\}$, are simulated over 50 rotations with $L_x = 20$ m and $\lambda = 4.5$. From the results shown in Figure 8, it is clear that increasing turbulence intensity elicits the greatest change in $\sigma_{C_{M_y}}$, and that isotropic turbulence produces similar fluctuations to anisotropic turbulence. Notably, there are no isolines showing where the ratio between $\bar{C}_{M_y}$ and $\bar{C}_{M_y(q.s)}$ exceeds unity, which indicates that turbulence in isolation does not affect the mean loads for a rotor operating at optimal λ.

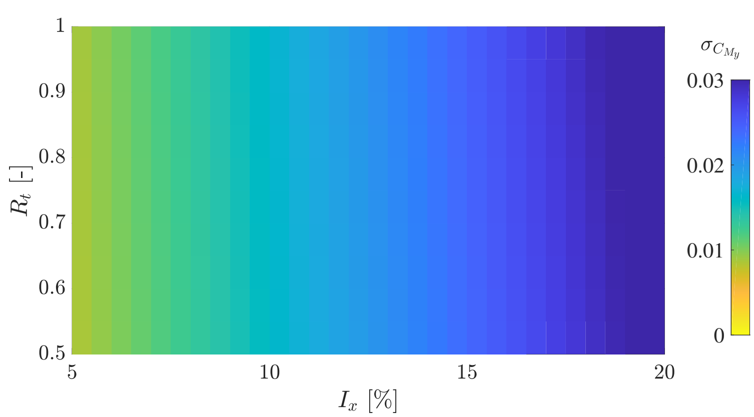

Figure 8: Filled contour map showing the standard deviation of the root bending moment due to varying turbulence intensity and anisotropy ratio.

4.3. Wave forcing

A tidal turbine will encounter a large range of waves with varying significant wave height (H_s) and apparent wave period (T_a). In our previous work we considered a measured time series from EMEC during the presence of large waves with $H_s = 5$ m and $T_a = 10$ s [7]. Here we model a range of waves to investigate the effect of amplitude, frequency and direction. We model wave particle velocities using Stokes second-order wave theory for monochromatic waves (see, for instance, Dean and Dalrymple [32]). The streamwise wave particle velocity is

$$u_x = \frac{gH_sK}{2\omega_a}\frac{\cosh K(z+d)}{\cosh(Kd)}\cos(Kx-\omega_a t)+\frac{3}{16}H_s^2\omega_a K\frac{\cosh 2K(z+d)}{\sinh^4(Kd)}\cos\Big(2(Kx-\omega_a t)\Big), \tag{15}$$

and the depthwise particle velocity (u_z) is

$$u_z = \frac{gH_sK}{2\omega_a}\frac{\sinh K(z+d)}{\cosh(Kd)}\sin(Kx-\omega_a t)+\frac{3}{16}H_s^2\omega_a K\frac{\sinh 2K(z+d)}{\sinh^4(Kd)}\sin\Big(2(Kx-\omega_a t)\Big), \tag{16}$$

where g is gravitational acceleration, K the wave number in m^{-1} and ω_a the angular wave frequency. The wave number is determined by solving (iteratively) the linear dispersion relation, including a Doppler shift to superimpose the effect of the current, given by

$$(\omega_a + KU_\infty\cos\theta)^2 = gK\tanh(Kd), \tag{17}$$

where θ is the oblique wave angle relative to U_∞. As with γ, the component perpendicular to the rotor becomes $u_x\cos(\theta)$ and a tangential azimuthally varying component ($u_x\sin\theta\cos\psi$) appears.

A number of waves are simulated with parameters, $H_s \in \{1, 6\}$ m, $T_a \in \{2, 12\}$ s and $\theta \in \{0, 180°\}$. The predicted $\sigma_{C_{M_y}}$ for all flow combinations are shown in Figure 9. We find that the load amplitude is proportional to T_a and, to a lesser extent, H_s. Waves following the tidal current ($\theta = 0$) lead to greater amplitude fluctuations at shorter wave periods, compared to waves opposing the current ($\theta = 180°$). The amplitude is significantly reduced for $\theta = 2\pi/5$ and $3\pi/5$. This is because the perpendicular velocity component becomes small for angles close to $\pi/2$. The isolines show that ratio between $\bar{C}_{M_y}$ and $\bar{C}_{M_y(q.s)}$ only exceeds unity for the most extreme waves.

These results confirm that T_a has more influence on blade loads than H_s and that the load amplitude is increased when waves follow the current.

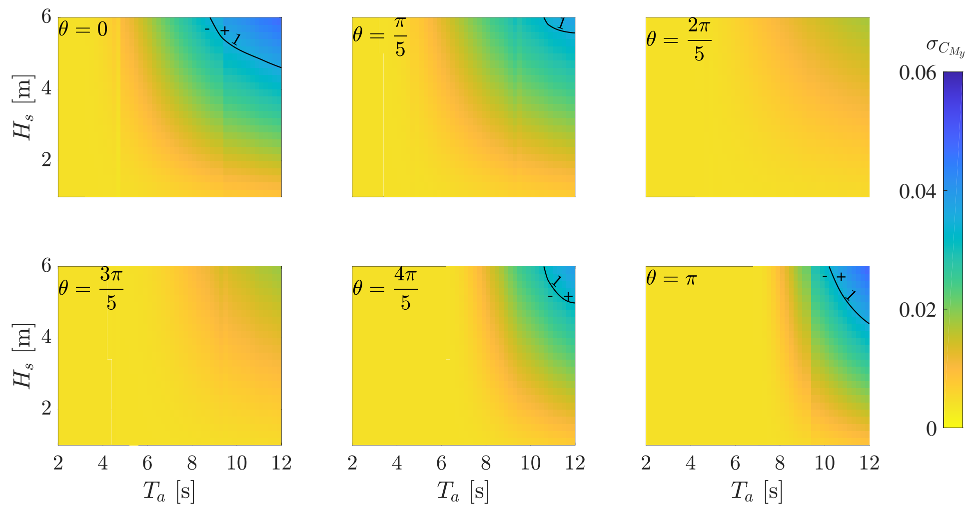

Figure 9: Filled contour map showing the standard deviation of the root bending moment due to varying wave period, wave height and wave direction. Solid contour lines show the ratio between the mean root bending moment and the quasi-steady counterpart.

4.4. Combined forcing

Combinations of shear, yaw, waves and turbulence are simulated to determine which combined flow condition produces the largest fluctuations. Informed by the results from the individual forcing tests, the flow parameters considered are: isotropic turbulence with $I_x = 0.1$ and $L_x = 20$ m, waves of $H_s = 5$ m, $T_a = 10$ s and $\theta = 0$ and a yaw misalignment of $\gamma = 30°$. The turbine operates at the optimum, $\lambda = 4.5$ and at the velocity for rated power, $U_0 = 2.7$ ms^{-1}. Shear is present for all cases, with $\nu = 1/7$.

A small correction is made to combine the effect of a yawed rotor sampling waves. When this happens, wave particle velocities either lead or lag relative to those experienced at the hub. We use the correction given by Galloway *et al.*

[13] where a lag t_x is applied to t in Equation 15 and Equation 16, which is defined as

$$t_x = \frac{r \sin\psi \sin\gamma}{U_\infty}. \tag{18}$$

The spectral method ensures that the expected value and standard deviation both remain constant. However, random phasing could potentially produce extraordinarily extreme values due to components combining or cancelling. To ensure extreme values are statistical significance we simulated 10^4 random samples and recorded the minimum ($\min u_x$) and maximum ($\max u_x$) velocities for each sample and determine a 95% confidence interval (CI). The sample histograms are shown in Figure 10, which are fitted to the generalised extreme value distribution. Using this distribution we computed the 95% CI for the

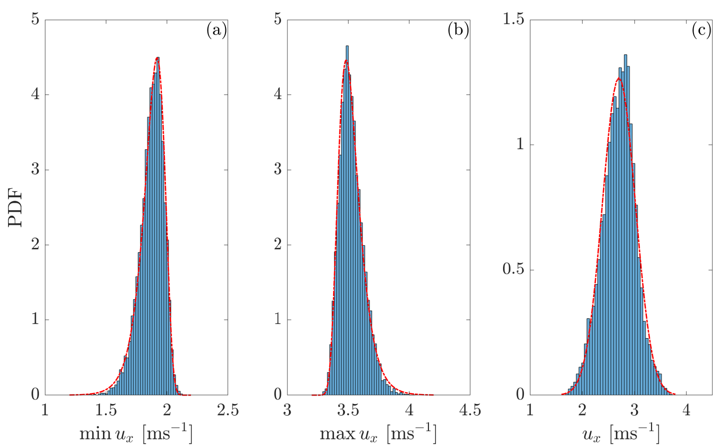

Figure 10: Histogram and generalized extreme value distribution fit for (a) the minimum turbulent velocity variation and (b) the maximum turbulent velocity variation. In (c) the velocity time series histogram is fitted to a normal distribution.

minimum and maximum values as [1.617 - 2.025] and [3.375 - 3.785], respectively. Ensuring that extreme values remain inside this 95% CI, ensures that a statistically significant case is used for comparison. In addition, identical turbulent times series are used for all cases. The extreme values for the sample we use are: $\min u_x = 1.864$ m^{-1} and $\max u_x = 3.488$ m^{-1}, which are comfortably inside the confidence interval. The histogram of the sample time series is shown in Figure 10 (c), which as shown approximately fits a normal distribution.

The distribution of C_{M_y} over 100 rotations are presented as a boxplot for each forcing. A boxplot shows the distribution of the quartiles as illustrated in Figure 11. The boxplots for the eight possible flow combinations are shown in Figure 12. As expected, shear in isolation produces the shortest C_{M_y} spread and the inclusion of a yaw misalignment reduces the median value and increases the spread. Turbulence significantly increases the spread and produces some very large outliers. The total spread of C_{M_y} due to waves is shorter than the turbulence case, however, the interquartile range (IQR), containing the 25th to 75th percentiles has the largest spread of the set. Combining waves with turbulence, produces the widest spread in the set (ignoring outliers). The further inclusion of a yaw misalignment with waves and turbulence produces both the minimum and maximum values in the set. Having identified that waves combined with

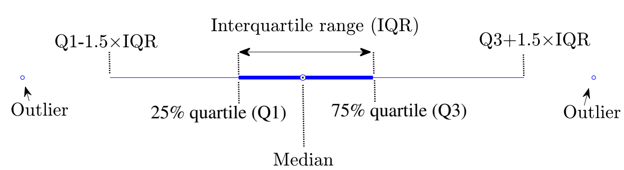

Figure 11: Box plot descriptor.

turbulence produce the largest C_{M_y} amplitude, a range of waves combined with turbulence are simulated with and without a yaw misalignment to determine which cases lead to $\bar{C}_{M_y(q.s)}$ overshoots. The predicted $\sigma_{C_{M_y}}$ are shown in Figure 13 (a) for $\gamma = 0$ and (b) for $\gamma = 30°$. Comparing the two cases, there is a small reduction in $\sigma_{C_{M_y}}$ across the full range for $\gamma = 30°$, confirming that a yaw misalignment reduces $\sigma_{C_{M_y}}$ when combined with waves and turbulence. The range and severity of $\bar{C}_{M_y(q.s)}$ overshoots for $\gamma = 0$ compared to waves without turbulence (Figure 9) is unchanged. Whereas for $\gamma = 30°$ both have increased, with more than a quarter of the test space affected.

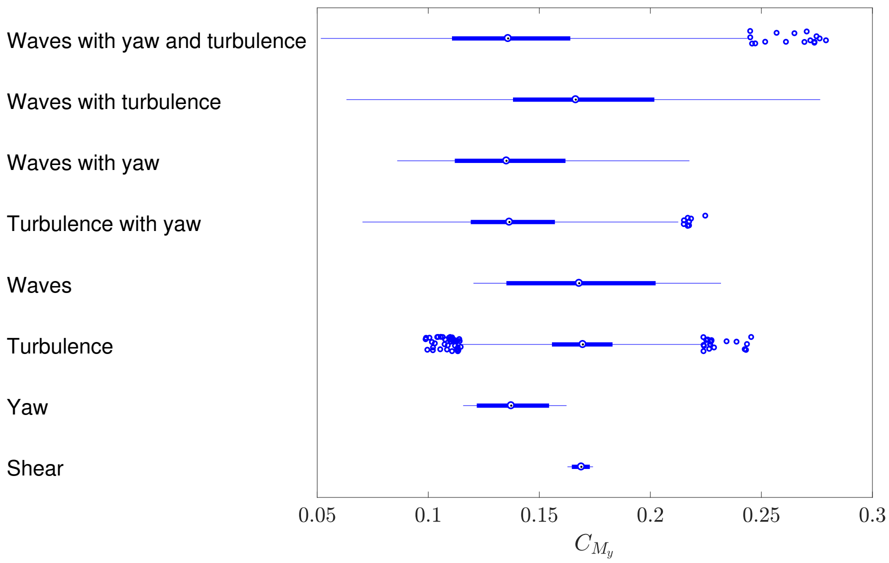

Figure 12: Box plot showing the summary statistics for the root bending moment time history over 50 blade rotations for several unsteady flow conditions. The circles indicate outliers.

5. Unsteadiness along the span

In this section we investigate how unsteadiness unfolds along the blade for different flow combinations and reveal which unsteady phenomena are occurring.

5.1. Unsteady loading from combined flow

The unsteady response at three span locations, tip ($r = 0.98R$), mid ($r = 0.56R$) and root ($r = 0.15R$), are analysed for each combined flow. Box plots shown in Figure 14 present the C_L summary statistics at each location. Notably, both the mean and the amplitude of C_L grow as we travel inboard from the tip, and become very large at the root. As with C_{M_y}, the mean value is reduced when the rotor is yawed. The case without a yaw misalignment (waves with turbulence), as expected, produces the largest median at each location. This also yields the widest spread at the tip and mid locations, however, conversely the shortest at the root. At the root the inclusion of a yaw misalignment induces extremely large fluctuations, especially when combined with turbulence. The case where all flow conditions are present leads to a maximum $C_L \approx 5$, which

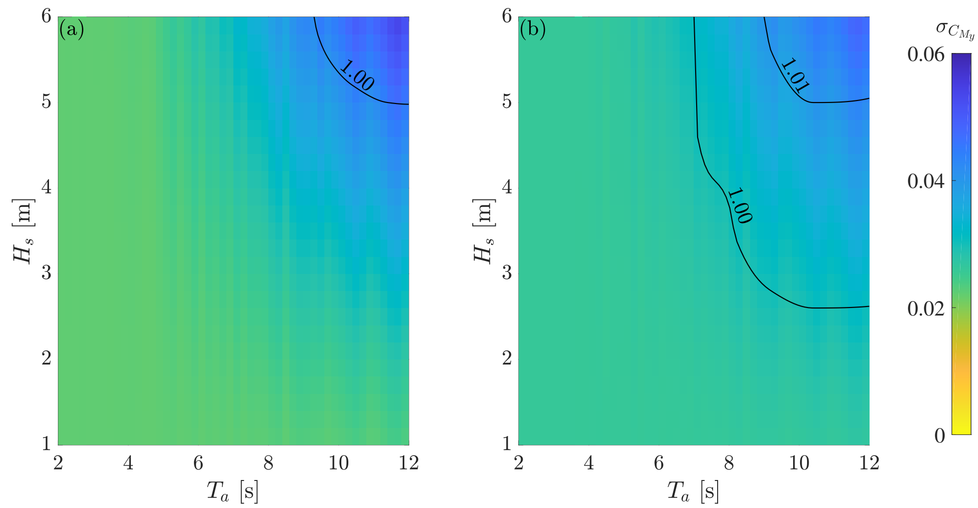

Figure 13: Filled contour map showing the standard deviation of the root bending moment due to varying wave period and wave height combined with turbulence for (a) zero yaw angle and (b) yaw angle of 30°. Solid contour lines show the ratio between the mean root bending moment and the quasi-steady counterpart.

is extreme. The reason being the very large α fluctuations arising from the slow tangential velocity, coupled with the tangential component induced by the rotor misalignment. This case also produces the widest spread along with the maximum and minimum values for the set. Interestingly, at the root, when turbulence and yaw combine, a much wider C_L spread than waves with yaw occurs. Waves combined with turbulence produces the smallest spread in the set, whereas this forcing produced the widest C_{M_y} spread (see Figure 12).

While the results in Figure 14 show the largest unsteady loadings in relative terms (relative to the local dynamic pressure), Figure 15 shows how these are relevant in absolute terms. Here we show the distributed thrust force (F_T) at the three blade locations. This force component is responsibly for M_y. The pattern is quite different from C_L. Notably, with dimensions considered, the median value decreases as we travel inboard from tip. The F_T spread is reduced at the root, which is most notable for yawed cases. There is little difference between the spread at the tip and mid sections, since the larger C_L at the mid

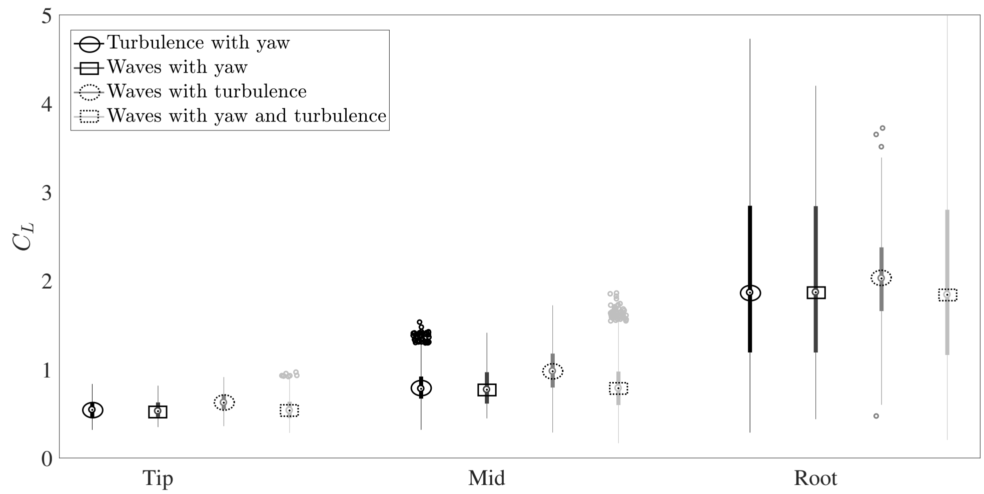

Figure 14: Box plot showing the summary statistics for the lift coefficient time history over 50 blade rotations for several unsteady flow conditions at the tip mid and root blade sections.

section counteracts the smaller U_r compared to the tip. The combination of waves with turbulence produces the largest median, peak and widest spread of the set, which, occurs at the mid-section.

5.2. Local unsteady characteristics

Here a visualisation of the unsteady phenomena discussed in section 3 is given for each of the four flow combinations by displaying on the blade: the location and duration of flow separation, leading edge vortex shedding, highly unsteady regions, where returning wakes are discernible and where added mass is significant. The frequencies used to compute k were determined by analysing the C_L frequency spectrum, whereby the three highest peaks at the tip, mid-section and root of the blade were selected.

The representative blades in Figure 16 show (a) turbulence and yaw, (b) waves and yaw, (c) waves, turbulence and yaw and (d) waves and turbulence. The results reveal that variation in the unsteady phenomena is dependent on the flow forcing. The flow becomes highly unsteady ($k > 0.2$) for every case, however, the transition point on the blade depends on the forcing. For $\gamma = 0$ (d) this occurs at the root of the blade, whereas for turbulence combined with a yaw

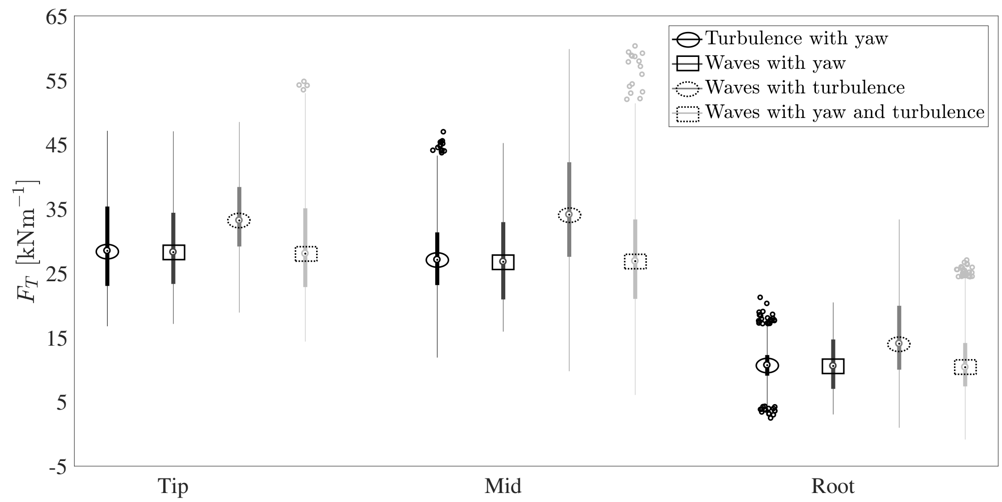

Figure 15: Box plot showing the summary statistics for the thrust force time history over 50 blade rotations for several unsteady flow conditions at the tip mid and root blade sections.

misalignment, transition occurs outboard of the mid-section. Interestingly, only two of the flow conditions have regions where added mass effects are significant ($k > 0.56$). These are when either turbulence (a) or waves (b) are combined with yaw misalignment. For blade (a) undergoing turbulence and yaw, the affected area is almost a quarter of the span. This case also contains the set maximum $k \approx 0.9$. Compared to blade (b), the affected region is only half the size and confined to the very bottom of the blade where the global effect is negligible due to the low relative velocity and short moment arm. In addition, the flow is separated inside these regions, thus, dynamic stall will govern the loading. We observe at the outer sections of each blade that the flow is attached and that $k < 0.3$. Therefore, returning wakes will give rise to slightly larger amplitudes than predicted by the model. Observing separated flow phenomena, it is clear that both regimes of dynamic stall (light and deep) occur on each blade. The blade without a yaw misalignment (d) contains the largest region of flow separation, spanning from the hub to $r \approx 6$ m. Deep dynamic stall, identified by the presence of the LEV, is mostly confined to the blade root. However, for waves with both turbulence and yaw (c) the region covers almost a third of the span. As shown in Figure 13, this leads to an overshoot in $\bar{C}_{M_y}$.

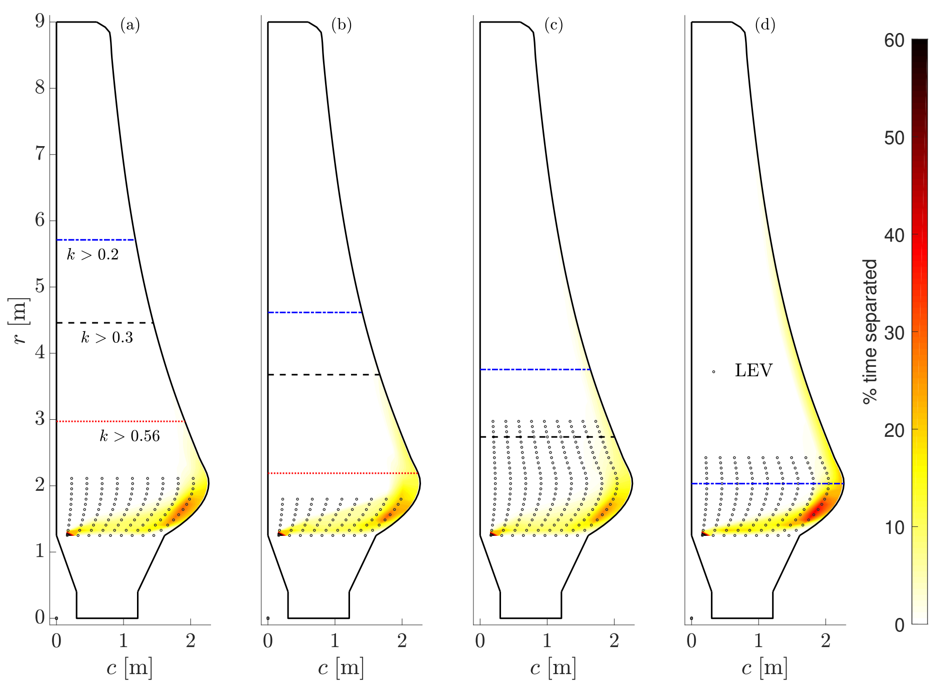

Figure 16: Parameterisation of unsteady effects along the blade, showing reduced frequency boundaries, dynamic stall and leading edge vortex shedding (indicated by black circles). The flow cases are; (a) turbulence and yaw, (b) waves and yaw, (c) waves, turbulence and yaw and (d) waves and turbulence.

5.3. Unsteady characteristics outside rated power

So far we have assumed that the turbine operates at rated power ($U_0 = 2.7\text{ms}^{-1}$). We now ask, how do the unsteady effects change below or above the rated velocity? Below rated power the turbine operates at the optimum tip-speed ratio, so the relative velocity will decrease as will the amplitude of the oscillations. So flow separation will be reduced. Above rated velocity the power must be controlled to match the rated value. If the device has a pitch mechanism, the blades are pitched towards the inflow to reduce α and C_L, whilst the rotor speed is kept constant [33]. If the turbine is without a pitch mechanism, the power can be actively controlled by reducing the rotor speed, referred to as

407 "underspeed" [34]. The latter will reduce λ. Referring back to Figure 6, we see from the solid isolines that this will lead to increased separation and dynamic stall. For a pitch regulated turbine the consequences are unclear. To investigate we reproduced the cases shown in Figure 16 with $U_0 = 3.2$ ms^{-1} and pitched the blades by 4.6°. The results presented in Figure 17 show that separation still occurs at the same locations on the blade but the duration has reduced. The severity of the unsteadiness in terms of k has also reduced due to the increase in U_r. For waves with turbulence (d),there are no sections undergoing highly unsteady oscillations ($k > 0.2$). The range of LEV shedding increases for all cases undergoing a yaw misalignment, whereas for the case without (d) the range decreases. Hence, for a pitch controlled turbine operating above rated velocity, LEV shedding would increase if a yaw misalignment is present.

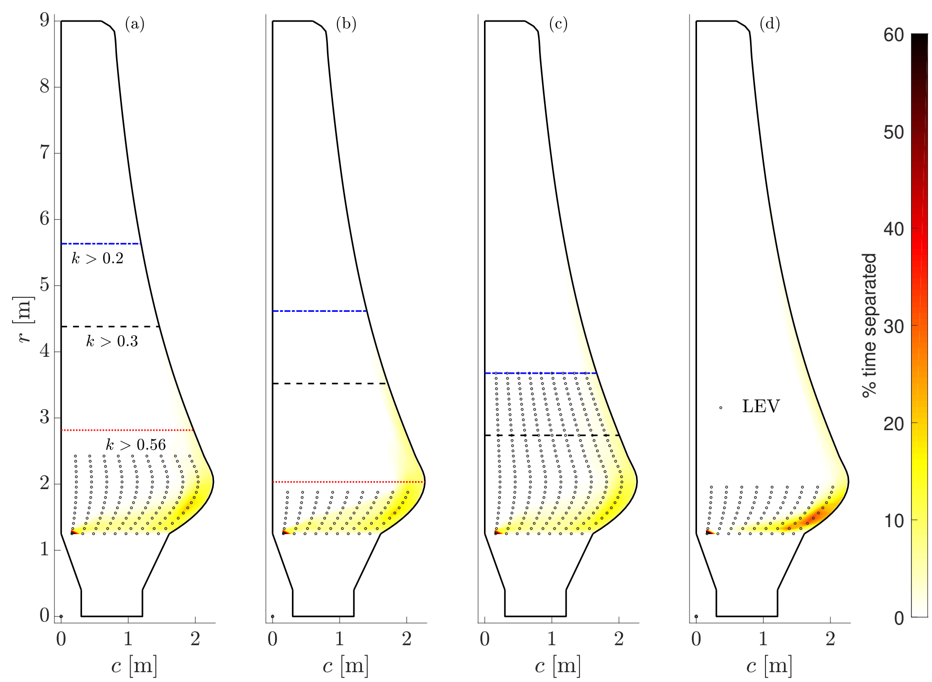

Figure 17: Parameterisation of unsteady effects along the blade for a pitch controlled turbine, showing reduced frequency boundaries, dynamic stall and leading edge vortex shedding (indicated by black circles). The flow cases are; (a) turbulence and yaw, (b) waves and yaw, (c) waves, turbulence and yaw and (d) waves and turbulence.

6. Conclusions

A better understanding of the unsteady loads encountered by a full-scale tidal turbine blade will aid the future development of tidal power. In this study we simulated loadings on the blade due to yaw, shear, turbulence and waves to determine which flow conditions induce the most significant load fluctuations on the blade and highlight which unsteady phenomena are occurring. Our results show that turbulence, waves or yaw misalignment can lead to load peaks that are twice the median load. The most significant root bending moment amplitudes are produced by large ($H_s > 2$ m), long period waves ($T_a > 5$ s) which follow the current, and that the amplitude is further increased when combined with turbulence ($I_x > 10\%$). In comparison, loadings caused by the blade rotating through the shear layer are negligible. Extreme waves ($H_s > 5$ m) dominate over extreme turbulence ($I_x > 15\%$). Large yaw angles ($\gamma > 30°$), low tip-speed ratios ($\lambda < 4$) and very large waves ($H_s > 5$ m) elicit overshoots in the time averaged blade root bending moment compared to the quasi-steady prediction. This indicates that dynamic stall is having a global affect. A yaw misalignment leads to larger fluctuations and a lower median value which in turn reduces the peak load. Locally, yaw induces extreme lift coefficients at the root of the blade. However, when dimensions are considered, the thrust force, which is normal to the blade, is larger at the tip than at the root. The largest thrust force occurs at the mid-section during large waves and turbulence.

Below a critical reduced frequency of 0.56, the added mass effects damp the total response, but above this value significant load fluctuation can occur. For the range of flow combinations experienced by tidal turbine blades, added mass effects mostly attenuated the load fluctuations and only became significant in the presence of a very large yaw misalignment. Flow separation is most prevalent with waves, leading to light dynamic stall (i.e. periodic trailing edge separation) over a large region of the blade. However, deep dynamic stall occurs for all flow combinations near the hub of the blade. These conclusions are valid for any tidal current velocity up to rated velocity, which produces the maximum power the turbine is designed for. When the current speed further increases, the power and the loads on the turbine must be kept constant to prevent failures. If the power is regulated fixing the rotational speed and pitching the blades to feather, then the effect of yaw misalignment becomes even more critical. In these conditions, the region affected by dynamic stall extends to half of the blade span.

We showed that turbulence, waves or yaw misalignment can lead to extreme load peaks. Moreover, low tip-speed ratios, as well as large yaw misalignment can cause the mean root bending moment to overshoot the mean value predicted by a quasi-steady approximation. For these reasons it is advisable that unsteady phenomena are always considered in the assessment of both the instantaneous and time-averaged loads on a turbine.

7. Acknowledgements

The first named author is supported by an Engineering and Physical Sciences Research Council studentship.

References

[1] Neill SP, Vögler A, Goward-Brown AJ, Baston S, Lewis MJ, Gillibrand PA, et al. The wave and tidal resource of Scotland. Renewable Energy 2017;114:3–17. doi:10.1016/j.renene.2017.03.027.

[2] Meygen LTD . MeyGen Tidal Energy Project Phase 1 Environmental Statement. Tech. Rep.; MeyGen; 2012. URL: https://tethys.pnnl.gov/sites/default/files/publications/MeyGen-2012-ES.pdf.

[3] Chen L, Lam WH. A review of survivability and remedial actions of tidal current turbines. Renewable and Sustainable Energy Reviews 2015;43:891–900. URL: 10.1016/j.rser.2014.11.071http://linkinghub.elsevier.com/retrieve/pii/S1364032114010107. doi:10.1016/j.rser.2014.11.071.

[4] Magagna D, Uihlein A. Ocean energy development in Europe: Current status and future perspectives. International Journal of Marine Energy 2015;11:84–104. URL: http://dx.doi.org/10.1016/j.ijome.2015.05.001http://linkinghub.elsevier.com/retrieve/pii/S2214166915000181. doi:10.1016/j.ijome.2015.05.001.

[5] McCroskey WJ. Unsteady Airfoils. Annual Review of Fluid Mechanics 1982;14:285–311. URL: http://www.annualreviews.org/doi/abs/10.1146/annurev.fl.14.010182.001441. doi:doi:10.1146/annurev.fl.14.010182.001441.

[6] Guntur S, Sørensen NN, Schreck S, Bergami L. Modeling dynamic stall on wind turbine blades under rotationally augmented flow fields. Wind Energy 2016;19(3):383–97. URL: http://onlinelibrary.wiley.com/doi/10.1002/we.1608/fullhttp://doi.wiley.com/10.1002/we.1839. doi:10.1002/we.1839. arXiv:arXiv:1006.4405v1.

[7] Scarlett GT, Sellar B, van den Bremer T, Viola IM. Unsteady hydrodynamics of a full-scale tidal turbine operating in large wave conditions. Renewable Energy 2019;143:199–213. URL: https://linkinghub.elsevier.com/retrieve/pii/S096014811930607X. doi:10.1016/j.renene.2019.04.123.

[8] Whelan J, Graham J, Pierø J. Inertia Effects on Horizontal Axis Tidal-Stream Turbines. Proceedings of the 8th European Wave and Tidal Energy Conference, Uppsala, Sweden 2009;:586–91.

[9] Milne IA, Day AH, Sharma RN, Flay RGJ. Blade loads on tidal turbines in planar oscillatory flow. Ocean Engineering 2013;60:163–74. URL: http://linkinghub.elsevier.com/retrieve/pii/S0029801812004465. doi:10.1016/j.oceaneng.2012.12.027.

[10] Milne IA, Day AH, Sharma RN, Flay RGJ. Blade loading on tidal turbines for uniform unsteady flow. Renewable Energy

2015;77:338–50. URL: http://linkinghub.elsevier.com/retrieve/pii/S0960148114008556. doi:10.1016/j.renene.2014.12.028.

[11] Theodorsen T. General theory of aerodynamic instability and the mechanism of flutter. NACA Technical Report 496 1935;:413 –33.

[12] Milne IA, Day AH, Sharma RN, Flay RGJ. The characterisation of the hydrodynamic loads on tidal turbines due to turbulence. Renewable and Sustainable Energy Reviews 2016;56:851–64. URL: http://linkinghub.elsevier.com/retrieve/pii/S1364032115013623. doi:10.1016/j.rser.2015.11.095.

[13] Galloway PW, Myers LE, Bahaj AS. Quantifying wave and yaw effects on a scale tidal stream turbine. Renewable Energy 2014;63:297–307. URL: http://www.sciencedirect.com/science/article/pii/S0960148113004977. doi:10.1016/j.renene.2013.09.030.

[14] Gretton GI. Development of a computational fluid dynamics model for a horizontal axis tidal current turbine. Tech. Rep. WG3 WP5 D1; 2010.

[15] Loewy RG. A two-dimensional approximation to the unsteady aerodynamics of rotary wings. Journal of the Aeronautical Sciences 1957;24(2):81–92.

[16] Leishman JG. Principles of Helicopter Aerodynamics. Cambridge University Press; 2006.

[17] McNae DM. Unsteady Hydrodynamics of Tidal Stream Turbines. Ph.D. thesis; Imperial College London; 2013.

[18] McCroskey W. Vortex wakes of rotorcraft. In: 33rd Aerospace Sciences Meeting and Exhibit. Reston, Virigina: American Institute of Aeronautics and Astronautics; 1995,URL: http://arc.aiaa.org/doi/10.2514/6.1995-530. doi:10.2514/6.1995-530.

[19] Sheng W, Galbraith RAM, Coton FN. A new stall-onset criterion for low speed dynamic-stall. Journal of Solar Energy Engineering 2006;128(4):461.

URL: http://solarenergyengineering.asmedigitalcollection.asme.org/article.aspx?articleid=1457809. doi:10.1115/1.2346703.

[20] Lindenburg C. Modelling of rotational augmentation based on engineering considerations and measurements. In: European Wind Energy Conference. 2004, p. 22–5.

[21] Scarlett GT, Viola IM. Tidal turbine hydrodynamic model. 2017. URL: https://github.com/gabscarlett.

[22] Ning AS. A simple solution method for the blade element momentum equations with guaranteed convergence. Wind Energy 2014;17:1327–45. URL: http://onlinelibrary.wiley.com/doi/10.1002/we.1608/fullhttp://doi.wiley.com/10.1002/we.1636. doi:10.1002/we.1636. arXiv:arXiv:1006.4405v1.

[23] Wagner H. Über die entstehung des dynamischen auftriebes von tragflügeln. Journal of Applied Mathematics and Mechanics/Zeitschrift für Angewandte Mathematik und Mechanik 1925;5(1):17–35.

[24] Janiszewska JM, Reuss Ramsay R, Hoffmann MJ, Gregorek GM. Effects of grit roughness and pitch oscillations on the S814 airfoil. Tech. Rep.; 1996. doi:10.2172/266691.

[25] Ning A, Hayman G, Damiani R, Jonkman JM. Development and validation of a new blade element momentum skewed-wake model within AeroDyn. In: 33rd Wind Energy Symposium. December 2014; Reston, Virginia: American Institute of Aeronautics and Astronautics. ISBN 978-1-62410-344-5; 2015,URL: http://www.nrel.gov/docs/fy15osti/63217.pdfhttp://arc.aiaa.org/doi/10.2514/6.2015-0215. doi:10.2514/6.2015-0215.

[26] Burton T, Jenkins N, Sharpe D, Bossanyi E. Wind Energy Handbook. Chichester, UK: John Wiley & Sons, Ltd; 2011. ISBN 9781119992714. URL: http://doi.wiley.com/10.1002/9781119992714. doi:10.1002/9781119992714.

[27] Diederich W, Franklin B, Field L. Effect of spanwise variations in gust intensity on the lift due to atmospheric turbulence. Tech. Rep.; NACA.; Langley; 1957.

[28] Shinozuka M. Monte Carlo solution of structural dynamics. Computers and Structures 1972;2(5-6):855–74. doi:10.1016/0045-7949(72)90043-0.

[29] Milne IA, Sharma RN, Flay RGJ, Bickerton S. Characteristics of the turbulence in the flow at a tidal stream power site. Philosophical Transactions of the Royal Society A: Mathematical, Physical and Engineering Sciences 2013;371(1985):20120196. URL: http://www.ncbi.nlm.nih.gov/pubmed/23319707{%}5Cnhttp://rsta.royalsocietypublishing.org/content/371/1985/20120196.short. doi:10.1098/rsta.2012.0196.

[30] Milne IA, Sharma RN, Flay RGJ. The structure of turbulence in a rapid tidal flow. Proceedings of the Royal Society A: Mathematical, Physical and Engineering Science 2017;473(2204):20170295. URL: http://rspa.royalsocietypublishing.org/lookup/doi/10.1098/rspa.2017.0295. doi:10.1098/rspa.2017.0295.

[31] Sellar B, Wakelam G, Sutherland DRJ, Ingram DM, Venugopal V. Characterisation of tidal flows at the European marine energy centre in the absence of ocean waves. Energies 2018;11(1):176. URL: http://www.mdpi.com/1996-1073/11/1/176. doi:10.3390/en11010176.

[32] Dean RG, Dalrymple RA. Water Wave Mechanics for Engineers and Scientists; vol. 2 of *Advanced Series on Ocean Engineering*. World Scientific Publishing Co. Pte. Ltd.; 1991. ISBN 9789812385512. URL: http://books.google.co.uk/books/about/Water{_}Wave{_}Mechanics{_}for{_}Engineers{_}and{_}S.html?id=9-M4U{_}sfin8C{&}pgis=1http://ebooks.worldscinet.com/ISBN/9789812385512/9789812385512.html. doi:10.1142/9789812385512.

[33] Whitby B, Ugalde-Loo CE. Performance of Pitch and Stall Regulated Tidal Stream Turbines. IEEE Transactions on Sustainable Energy 2014;5(1):64–72. URL: http://ieeexplore.ieee.org/document/6578587/. doi:10.1109/TSTE.2013.2272653.

[34] Arnold M, Biskup F, Cheng PW. Load reduction potential of variable speed control approaches for fixed pitch tidal current turbines. International Journal of Marine Energy 2016;15:175–90. URL: http://dx.doi.org/10.1016/j.ijome.2016.04.012. doi:10.1016/j.ijome.2016.04.012.